A parametric investigation of AlGaAs/GaAs modulation-doped quantum wires

M. E. Sherwin and T. J. Drummond
Department of Electrical Engineering and Computer Science, University of Michigan, Ann Arbor, Michigan 48109-2122

(Received 3 July 1989; accepted for publication 28 August 1989)

Poisson's and Schrödinger's equations have been simultaneously solved in cylindrical coordinates for the problem of a cylindrical modulation-doped quantum well, also referred to as a quantum wire. A transfer matrix method for the solution of Schrödinger's equation has been implemented for cylindrical coordinates. For the case of a GaAs wire embedded in an AlGaAs host, a parametric investigation was undertaken to determine the effects of aluminum fraction, temperature, well radius, barrier doping, and spacer layer thickness upon the linear electron density within the quantum wire. Transferred electron densities in excess of 10^6 electrons per cm are easily achievable for a wide range of parameters.

I. INTRODUCTION

Semiconductor systems in which electrical transport is constrained by quantum-size effects in one, two, and three dimensions are referred to as quantum wells, quantum wires, and quantum dots, respectively. Epitaxially defined quantum-well structures have been studied extensively over the last decade and are now widely employed in modulation-doped field-effect transistors and multiple-quantum-well lasers. By imposing lateral definition on quantum-well structures, it is possible to create practical quantum-wire structures as evidenced by several recent reports.[1,2] By extension of the considerations which make quantum-well transistors and lasers superior to their bulk counterparts, quantum-wire devices are expected to demonstrate certain advantages over their quantum-well counterparts.

In the case of electronic devices, one-dimensional conductive channels are predicted to result in a closer approach to ballistic transport. Due to the barrier potential and the application of momentum conservation rules, scattering is greatly reduced in a one-dimensional system.[3-5] This paper considers the case of an *n*-type modulation-doped quantum wire, wherein large linear densities are obtained within the well, while the donor atoms reside in the confining barrier layer. The consequent minimization of Coulomb scattering is a further step in the direction of ballistic transport. In the case of *p*-type quantum wires, it has been theorized elsewhere that the hole effect mass will be significantly reduced along the wire even in the absence of strain.[6] In either case, ballistic or near-ballistic transport will be required in a practical transistor application. Due to the small cross-sectional area of the channel, the total number of electrons available for transport is very small. To obtain useful current densities requires either large saturated drift velocities or massive quantum-wire arrays.

Quantum wires have also been receiving some attention for their possible use as semiconductor lasers. The one-dimensional density of states should provide lasers with lower threshold currents. The density of states (DOS) is inversely proportional to the square root of the energy, as measured from each of the bound states. This arrangement of the DOS is advantageous for high-efficiency pumping. Since the DOS is also highest at the subband edges, it is easier to achieve inversion, and the output will be more nearly monochromatic than conventional semiconductor lasers. As with electrical devices, these quantum-wire lasers will not be able to generate a great deal of output power. However, because of their high efficiency and low power consumption, they may prove to be ideal for integrated optoelectronic computing circuits.

The work presented in this paper is intended to provide a parametric description of the *n*-type modulation-doped AlGaAs/GaAs quantum-wire system. This system is chosen because it is the easiest to deal with from a material and fabricational viewpoint. A realistic description requires the self-consistent solution of Poisson's and Schrödinger's equations. These equations are formulated in a cylindrical coordinate system to obtain a solution in terms of a single radial variable. Although square or triangular geometries might be more appropriate, the results should be qualitatively the same. In choosing a cylindrical coordinate system, we do unfortunately introduce a r^{-1} singularity at the origin which makes the implementation of popular numerical methods for solving Schrödinger's equation, such as the tridiagonal matrix method and Numerov's method, difficult if not impossible. In Secs. II, III, and IV, we describe an algorithm for solving Poisson's and Schrödinger's equations using a transfer matrix method for the solution of Schrödinger's equation. In Sec. V, the transferred electron density in the quantum wire is calculated for a wide range of dimensional and material parameters. The parameter space was chosen to represent the largest space of interest for both physical and device applications.

II. POISSON'S EQUATION

To obtain the electrostatic potential within and surrounding the quantum wire, one is required to solve Pois-

 0021-8979/89/235444-12$02.40

son's equation (1). Assuming there is no angular or z-axis dependence, Poisson's equation is decomposed into its constituent relations defining the electric field:

$$\nabla^2 V(r) = \frac{1}{r}\frac{d}{dr} r \frac{dV(r)}{dr} = -\frac{\rho(r)}{\epsilon(r)}, \tag{1}$$

$$\nabla \cdot \mathbf{E}(r) = \frac{1}{r}\frac{d}{dr} r\mathbf{E}(r) = \frac{\rho(r)}{\epsilon(r)}, \tag{2}$$

$$\nabla V(r) = \frac{dV(r)}{dr} = -\mathbf{E}(r). \tag{3}$$

The radial coordinate is partitioned into thin cylindrical shells surrounding a core region of radius r_c. $V(r)$ is assumed constant throughout the core, and $\rho(r_c)$ is calculated with reference to the Fermi energy, defined at $r = \infty$ by the doping level in the AlGaAs. Taking ρ to be constant within each shell, $\mathbf{E}(r)$ is defined within each shell by Eq. (2), and $V(r)$ at the outer boundary of the shell is calculated from Eq. (3). A correct choice of $V(r_c)$ implies that $\mathbf{E}(r) \to 0$ as $r \to \infty$. A representative solution is shown in Fig. 1.

A. The charge density ρ

There are two components making up the total charge density: electrons bound to the quantum well and the volume charge due to doping. The bound charge distribution is determined by Schrödinger's equation, having the units of C/cm, and the volume charge density, having units of C/cm^3. The volume charge is the net sum of free electrons, free holes, ionized donors, and ionized acceptors external to the quantum wire. The use of a line charge density for the bound electrons reflects the fact that perpendicular to the axis of the well, the spatial distribution of charge is a measure of the spatial distribution of a single electron at some point on the axis as a weighted average over all possible configurations (eigenfunctions).

The solution of Schrödinger's equation results in the energies and wave functions of the bound states. Using the energies and the spatially constant Fermi level, we can calculate the number of electrons associated with each bound state in the wire. As discussed later, the charge distribution within the well is determined by the wave functions associated with each bound state. Due to the two-dimensional confinement of the quantum wire, the density of states for the bound electrons is one-dimensional:

$$N(E)dE = \sqrt{\frac{2m^*}{h^2 E}}\, dE, \tag{4}$$

where h is Plank's constant and m^* is the effective mass for electrons in the bound states, assumed to be $0.067 m_0$.

Treating the AlGaAs conduction-band edge at $r = \infty$ as the zero reference of potential energy, we can write the following equation for the total number of electrons bound to this energy level:

$$n_j = \int_{E_j}^{\infty} N(E) f(E) dE = \sqrt{\frac{2m^*}{h^2}} \int_{E_j}^{\infty} \frac{E^{-1/2} dE}{1 + \exp[(E - E_f)/kT]}, \tag{5}$$

where k is Boltzmann's constant, E_j is the energy of the jth bound state, and E_f is the Fermi energy.

An analytic approximation for the Fermi integral described in Ref. 7 is used to obtain the following expression for the linear density of electrons. This approximation is accurate to within 1.2% for $-\infty < \eta < +\infty$:

$$n_j = \sqrt{\frac{2m^* kT}{h^2}} \times \left(\frac{\sqrt{2}/2}{[b + \eta + (|\eta - b|^c + a^c)^{1/c}]^{1/2}} + \frac{e^{-\eta}}{\Gamma(\frac{1}{2})} \right)^{-1}, \tag{6}$$

where

$$a = 1.697\,42,$$

$$b = 1.495,$$

$$c = 2.828\,43,$$

and

$$\eta = -[(E_f - E_j)/kT].$$

The variables a, b, and c are specified for the Fermi integral of order $-\frac{1}{2}$.

Now that we have an expression for the bound-electron density, we must consider the spatial distribution of the bound charge. The distribution of bound charge is proportional to the probability distribution which, in turn, is proportional to the square of the wave function $|\psi(r,\theta)|^2$. As will be evident later, $|\psi|^2$ is independent of θ, and we need consider only the radial distribution. In any differential region, we integrate $|\psi(r)|^2$ from r to $r + dr$ and normalize by the total distribution, i.e., $\int_0^\infty |\psi(r)|^2 r\, dr$. Integrating the probability over one shell and multiplying by the total number of electrons bound to that state gives the electron density within the shell. Multiplying the electron density by q, the electron charge, will give the charge density within the shell, as expressed by Eq. (7):

$$\rho(r) = q \sum_j n_j \frac{\int_r^{r+dr} \psi_j^2 2\pi r\, dr}{\int_0^\infty \psi_j^2 2\pi r\, dr}. \tag{7}$$

In the regions where the electrons are not bound due to quantum confinement, the net charge density is assumed to

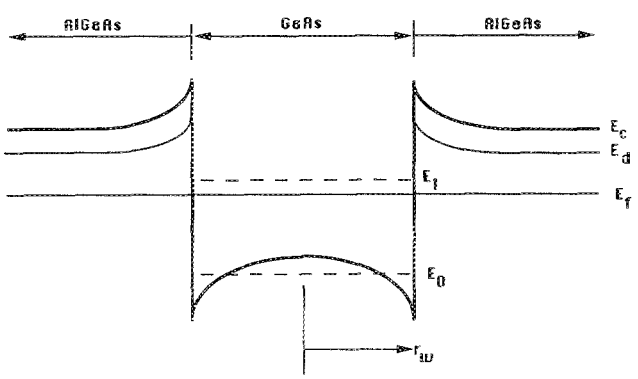

FIG. 1. A representative cross section of a quantum wire, with two bound states and a donor level. Only the conduction band is shown.

obey three-dimensional statistics. The material data that was used for GaAs and AlGaAs is listed in Appendix A. For the material outside of the well, the electron and hole density of states is three-dimensional and is given by the following equation:

$$N(E)dE = \frac{1}{2\pi^2}\left(\frac{2m^*}{\hbar^2}\right)^{3/2} E^{1/2}, \tag{8}$$

where m^* is the density-of-states effective mass and $\hbar$ is Plank's constant divided by 2π. The evaluation of the free-electron density is straightforward, assuming a multiconduction-band model. Each of the conduction-band minima will have an effect on the overall electron density in various composition ranges. As evident in Fig. 2, the Γ and X minima will dominate for low and high mole fractions, respectively, while all minima will contribute near the direct-indirect crossover. Including the effects of all three minima results in the following equation for the free-electron concentration:

$$n = N_c^{\Gamma} * F_{1/2}(\eta_{\Gamma}) + N_c^{X} * F_{1/2}(\eta_X) + N_c^{L} * F_{1/2}(\eta_L), \tag{9}$$

where $F_{1/2}$ is the half-order Fermi integral, and N_c^i is given by

$$N_c^i = \frac{4}{\sqrt{\pi}}\left(\frac{2\pi m_n^i kT}{h^2}\right), \tag{10}$$

where m_n^i is the density-of-states effective mass for the ith band.

Using the approximation in Ref. 7, we can write the half-order Fermi integral as follows:

$$F_{1/2}(\eta) = \left(\frac{3\sqrt{2}}{[b+\eta+(|\eta-b|^c+a^c)^{1/c}]^{1/2}} + \frac{e^{-\eta}}{\Gamma(\frac{1}{2})}\right)^{-1} \tag{11}$$

where

$a = 2.584\,81,$

$b = 2.105,$

$c = 2.414\,21,$

and

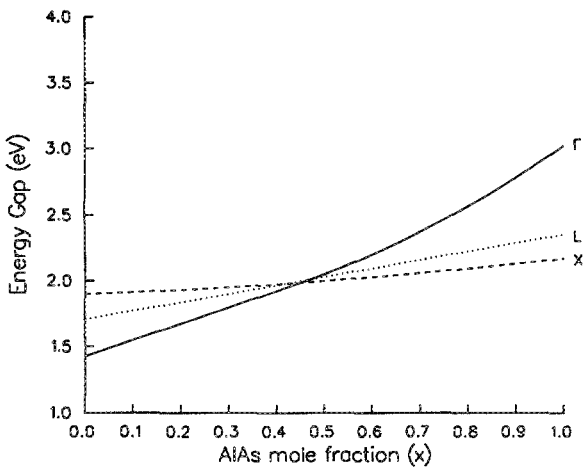

FIG. 2. Conduction-band minima vs aluminum arsenide mole fraction x in $Al_xGa_{1-x}As$.

$$\eta = -(E_f - E_c^i)/kT,$$

where E_c^i is the position of the ith conduction-band minimum and $i = \Gamma, L, X$. Using Eqs. (9) and (11), we can obtain a fairly accurate description of the free-electron concentration in the AlGaAs. As we are concerned with n-type modulation doping, we assume a simple description of the valence-band holes. Using a single density-of-states effective mass and a single valence band, we arrive at the following expression for the hole concentration:

$$p = 2\left(\frac{2\pi m_p^* kT}{h^2}\right)^{3/2} \exp\left(-\frac{E_f - E_v}{kT}\right), \tag{12}$$

where m_p^* is the valence-band density-of-states effective mass and E_v is the valence-band energy.

The final components of the volume charge are the ionized donors and acceptors. These are most easily modeled by assuming a single donor/acceptor ionization energy. A more complete model would have to include the effects of overlap between the donor states and the conduction band, but these effects are not of primary concern in this case. Reference 8 gives the following equations for the ionized donor/acceptor concentrations:

$$N_d^+ = \frac{N_{d0}}{1 + 2\exp[-(E_f - E_d)/kT]}, \tag{13}$$

$$N_a^- = \frac{N_{a0}}{1 + 4\exp[-(E_a - E_f)/kT]}, \tag{14}$$

where N_{d0} is the concentration of chemical donors, N_{a0} is the concentration of chemical acceptors, E_d is the donor energy level, and E_a is the acceptor energy level. The volume charge density is assumed to depend only on r as determined by Eqs. (15) and (1):

$$\rho(r) = q[N_d^+(r) + p(r) - n(r) - N_a^-(r)]. \tag{15}$$

B. The electric field

The electric field is found by integrating Eq. (2). Since the total charge density is made up of bound charge, with the units of C/cm, and the volume charge, with the units of C/cm^3, we will need to use two separate integrals. In solving Schrödinger's equation, the potential is assumed constant over the width of each shell. To solve Poisson's equation within the well, we must choose the thickness of the shells to be sufficiently thin, so that $\rho(r)$ is approximately constant across the shell. Averaging this term across the shell, rather than evaluating it numerically, reduced the computing time by a factor of 30, using FORTRAN on an Apollo 3500. Using Eqs. (7) and (15), describing the total charge within a shell, we develop Eq. (16) for the electric field at the outer edge of the shell, with reference to the electric field at the inner edge of the shell. The ith point is at the outer radius, while the $(i-1)$th point represents the inner radius. The ratio of dielectric constants is necessary for the case when the shell crosses the boundary between the GaAs well and the AlGaAs buffer region:

$$E_i = E_{i-1}\frac{r_{i-1}\epsilon_{i-1}}{r_i\epsilon_i} - \frac{q(r_i - r_{i-1})}{2\pi\epsilon_i r_i} \times \sum_{j=1}^{j_{\max}} (n_j\psi_j^2 2\pi r)_{\text{avg}} + \frac{q}{2\epsilon_i} \times (N_d^+ + p - n - N_a^-)\left(r_i - \frac{r_{i-1}^2}{r_i}\right), \quad (16)$$

where the summation is to be carried out over the total number of bound states ($j_{\max}$), and n_j is the total number of electrons bound to the jth subband in the quantum wire.

C. The potential

Obtaining an equation for the potential $V(r)$ is simply a matter of integrating Eq. (16) across the shell. Equation (3) gives the relationship between the potential and the electric field. In the previous calculations, the electric field has been treated as being negative; so we can remove the negative sign in Eq. (3). If we treat the electric field in Eq. (16) as being a function of r between r_{i-1} and r_i, and treating the integration variable as r_i, we arrive at Eq. (17). As before, we assume that the charge density is constant across each shell:

$$V_i = V_{i-1} + \int_{r_{i-1}}^{r_i} E(r_i')dr_i',$$

$$V_i = V_{i-1} + \left(E_{i-1}\frac{r_{i-1}\epsilon_{i-1}}{\epsilon_i}\right)\ln\left(\frac{r_i}{r_{i-1}}\right) + \frac{q(N_d^+ + p - n - N_a^-)}{2\epsilon_i} \times \left[\frac{r_i^2 - r_{i-1}^2}{2} - r_{i-1}^2\ln\left(\frac{r_i}{r_{i-1}}\right)\right] - \frac{q[(r_i - r_{i-1}) - r_{i-1}\ln(r_i/r_{i-1})]}{2\pi\epsilon_i} \times \sum_{j=1}^{j_{\max}} (n_j\psi_j^2 2\pi r)_{\text{avg}}, \quad (17)$$

where the summation is to be carried out over the total number of bound states ($j_{\max}$), and n_j is the total number of electrons bound to the jth band.

III. SCHRÖDINGER'S EQUATION

The solution of Schrödinger's equation for an arbitrary potential is easily solved in Cartesian coordinates. In cylindrical coordinates there is a singularity in the equation at $r = 0$, which can cause numerical instabilities. The general form of Schrödinger's equation is shown below:

$$-(\hbar^2/2m)\nabla^2\psi + V\psi = E\psi. \quad (18)$$

For the cylindrical quantum well, V is only a function of r, and the method of separation of variables[9] can be used to solve for the radial and angular equations separately. The potential is constant in the z direction and yields a free-electron-like dispersion. Setting $\psi(r,\theta) = R(r)\Theta(\theta)$. Equation (18) becomes

$$-\frac{\hbar^2}{2m}\left[\frac{r}{R}\frac{d}{dr}\left(r\frac{dR}{dr}\right) + \frac{1}{\Theta}\frac{d^2\Theta}{d\theta^2}\right] = [E - V(r)]r^2. \quad (19)$$

The angular portion of the equation becomes

$$\frac{d^2\Theta}{d\theta^2} = -n^2\Theta, \quad (20)$$

$$\Theta(\theta) = \exp(in\theta). \quad (21)$$

Using Eq. (20) and regrouping terms, we arrive at the final form of the radial equation:

$$\frac{d^2R}{dr^2} + \frac{1}{r}\frac{dR}{dr} - n^2R = \frac{2m}{\hbar^2}[V(r) - E]R. \quad (22)$$

The solution of the radial equation will produce the bound energies and the wave functions necessary for the solution of Poisson's equation. Since we wish to solve the radial equation for an arbitrary $V(r)$, we cannot solve Eq. (22) analytically, and we must look to various numerical methods.

A. The tridiagonal matrix method and Numerov's method

Both the tridiagonal matrix method and Numerov's method are relatively simple and well understood. Both of these work very well in Cartesian coordinates, but suffer problems with the singularity at $r = 0$ in cylindrical coordinates.

Equation (22) can be transformed into a finite-difference equation, having terms involving the ith, $(i-1)$th, and $(i+1)$th points. Evaluating this equation at a series of points across the well and barrier results in a tridiagonal matrix, which can be solved for the eigenfunctions and eigenvalues. One of the problems with this method is that the wave function is only determined at the input points and must be interpolated between these points. If a large number of points are desired, the computing time will increase dramatically. Furthermore, this method is incapable of handling the $1/r$ term in the radial equation and gives results which are highly sensitive to choice of step size and minimum r.

Numerov's method[10] is a form of a shooting solution to a second-order differential equation. The first step is to guess the energy of the bound state. Then an initial point of the wave function is chosen at large r, and using the radial equation, this solution is propagated inwards until $r = 0$. The value of the wave function at $r = 0$ determines if the energy guess is valid or not. This method is very simple to implement and usually solves for the energies in a short period of time. One difficulty with this method is the choice of an outer radius. The solved energy can change if the solution is started at different radii. Furthermore, as the $1/r$ term in the radial equation will diverge near $r = 0$ and cause difficulty in propagating the solution across the last few data points.

The tridiagonal matrix method is completely unsuitable for cylindrical coordinates, and Numerov's method becomes very difficult to implement in cylindrical coordinates. Although it is possible to use Numerov's method across singularity points,[11] it was easier to explore alternate techniques for the solution of the radial equation with an arbitrary potential.

B. Transfer matrix methodology for the solution of the radial equation

The development of this method was based on an earlier analysis of an ideal finite cylindrical quantum wire.[12] The two-region potential was constant within and external to the wire, with each region having a characteristic effective mass. This approach is generalized to a multiregion model with the radial partition defined as for the solution of Poisson's equation. Poisson's equation defines the potential at the boundaries of each shell; the average potential within each shell defines the value used to propagate Schrödinger's equation across the shell. In our case, at least 75 shells are required for a stable simultaneous solution of the two equations. Rewriting the radial equation (22), and defining the propagation/decay constant κ or χ, we arrive at Eq. (24). The subscript i refers to the shell number:

$$\kappa_i^2 = -\chi_i^2 = (2m_i/\hbar^2)(E - V_i), \tag{23}$$

$$\frac{d^2R}{dr^2} + \frac{1}{r}\frac{dR}{dr} + \left(\kappa_i^2 - \frac{n^2}{r^2}\right)R = 0. \tag{24}$$

The solutions to Eq. (24) are well known[13] and are various types of Bessel functions. If, within a layer, the chosen energy E is larger than V_i, then the solution will be oscillatory in nature. But if the energy is less than V_i, the solution will be indicative of decay. The two solution types are given in Eq. (25):

$$R_i(r) = \begin{cases} AJ_n(\kappa_i r) + BN_n(\kappa_i r), & \text{if } E \geqslant V_i, \\ CI_n(\chi_i r) + DK_n(\chi_i r), & \text{if } E \leqslant V_i. \end{cases} \tag{25}$$

Equation (25) defines only the wave function within each shell. Solution of the eigenenergies is obtained in a manner similar to that of Numerov's method. A guess is made at the energy within the core for $r < r_c$, and the wave function is propagated outward, matching the coefficients A,B or C,D at the boundary of each shell. An eigenenergy is identified with a wave function that asymptotically approaches zero as $r \to \infty$. This is true for all bound states with $E < 0$ as $r \to \infty$.

The first step before propagating the solution out from $r = 0$ is to set up the wave function in the first region, the region that includes the point $r = 0$. The first region can either be oscillatory or decay, but the wave function must be finite at all r. The Neumann function N_n and the function K_n both go to infinity as r approaches zero. Therefore, in the first region, the coefficient B or D must be equal to zero, depending if $E > V_1$ or $E < V_1$. Figure 1 shows the two possible cases for the lowest energy level; the energy can be less than V at $r = 0$. At large r, the potential is referenced to zero volts. Since we are only solving for true bound-state solutions, we need only to look for solutions with E less than zero.

In the final region, we know that solutions must be of the decay type and are therefore made up of the functions I_n and K_n. At larger r, the function I_n will diverge to infinity, and therefore the coefficient C should be zero. However, we do not set C to be zero, but search for energies that force C to zero in the last region. When solving this problem, the limits of computer accuracy must be taken into account. Even with double precision on an Apollo 3500, the energy can only be determined to 17 digits. Although this would seem sufficient, problems arise due to the exponential form of I_n. Unless the coefficient C is exactly zero, the wave function will eventually begin to grow again. Because of the limited number of digits, it is impossible to force C to be exactly zero, and the solution must be truncated at some point.

In order to propagate the solution from layer to layer, it is necessary to enforce various boundary conditions. The two boundary conditions that the wave function $R(r)$ must satisfy are (1) continuity of the wave function and (2) conservation of flux. If the boundary between successive layers is located at $r = a$, the boundary conditions are given by Eqs. (26) and (27):

$$R_l(a) = R_r(a), \tag{26}$$

$$\frac{R_l'(a)}{m_l(a)} = \frac{R_r'(a)}{m_r(a)}, \tag{27}$$

where the primes denote radial derivatives, and the subscripts l and r denote the left- and right-hand sides of the boundary, respectively.

Defining an oscillatory region as type I and a decay region as type II, there are four different cases that need to be treated. The boundaries can involve any of the following combinations: I-I, I-II, II-I, or II-II. As an example, the boundary equations for the I-II interface are developed, and the reader is referred to Appendix B for the other cases. The wave functions for the two regions are given below:

$$R_l(r) = AJ_n(\kappa_l r) + BN_n(\kappa_l r), \tag{28}$$

$$R_r(r) = CI_n(\chi_r r) + DK_n(\chi_r r). \tag{29}$$

The first step is to apply the boundary conditions [Eqs. (26) and (27)]:

$$AJ_n(\kappa_l a) + BN_n(\kappa_l a) = CI_n(\chi_r a) + DK_n(\chi_r a), \tag{30}$$

$$m_r[AJ_n'(\kappa_l a) + BN_n'(\kappa_l a)] = m_l[CI_n'(\chi_r a) + DK_n'(\chi_r a)]. \tag{31}$$

Now we need to solve for the unknowns, C and D. Since we are propagating outwards, we already know the values of A and B:

$$C = \frac{A[m_r J_n'(\kappa_l a)K_n(\chi_r a) - m_l J_n(\kappa_l a)K_n'(\chi_r a)]}{m_l I_n'(\chi_r a)K_n(\chi_r a) - m_l I_n(\chi_r a)K_n'(\chi_r a)} + \frac{B[m_r N_n'(\kappa_l a)K_n(\chi_r a) - m_l N_n(\kappa_l a)K_n'(\chi_r a)]}{m_l I_n'(\chi_r a)K_n(\chi_r a) - m_l I_n(\chi_r a)K_n'(\chi_r a)}, \tag{32}$$

$$D = \frac{A[m_r J_n'(\kappa_l a)I_n(\chi_r a) - m_l J_n(\kappa_l a)I_n'(\chi_r a)]}{m_l K_n'(\chi_r a)I_n(\chi_r a) - m_l K_n(\chi_r a)I_n'(\chi_r a)} + \frac{B[m_r N_n'(\kappa_l a)I_n(\chi_r a) - m_l N_n(\kappa_l a)I_n'(\chi_r a)]}{m_l K_n'(\chi_r a)I_n(\chi_r a) - m_l K_n(\chi_r a)I_n'(\chi_r a)}. \tag{33}$$

Using Eqs. (32) and (33) and similar equations in Appendix B, we can propagate the solution outwards from $r = 0$ to the last region. By minimizing the value of the wave function in the last region, it is very easy to determine the energy to at least six significant digits.

Although this method can be very accurate in its energy determination, the ultimate accuracy depends on the num-

ber of layers used in the approximation of a continuous potential. Figure 3 shows the results for a 5-nm-radius cylindrical quantum well. It is easy to see the importance of shell thickness of the final results. It is most important to have a large number of shells within the well and the closest portion of the barrier. Beyond twice the well radius, the shell size can be increased without a significant loss of accuracy.

IV. SOLUTION DEVELOPMENT AND EQUILIBRIUM

Equations (16) and (17) relate the electric field and potential across a single shell. The core must be treated independently. The electric field and potential cannot be evaluated at $r = 0$ due to inverse and logarithmic dependence on the radius, respectively. This problem leads us to define a cutoff radius r_c. All of the charge within the cutoff radius will be used in the evaluation of the initial electric field, and the potential will be assumed constant within the cutoff radius. Fortunately, the solution of this problem is not heavily dependent on the choice of the cutoff radius. Three angstroms is chosen for the cutoff radius, as this is roughly the nearest neighbor distance in the lattice.

The potential at the cutoff radius is the adjustable parameter in the search for equilibrium. Having assumed a value at V at r_c, the bound charge and volume charge can be evaluated within the 0.3-nm cutoff radius. The initial electric field is given below, neglecting the amount of ionized donors or acceptors within the cutoff radius:

$$E_1 = \frac{-q}{2\pi\epsilon_1 r_c} \sum_{j=1}^{j_{\max}} n_j \int_0^{r_c} \psi_j^2 2\pi r\, dr, \tag{34}$$

where r_c is 0.3 nm and $j_{\max}$ is the total number of bound states.

Equilibrium is defined as the state in which the electric field and the potential go to zero as r approaches ∞. In practice, it is nearly impossible to have both the electric field and the potential equal to zero at the same time. It is usually sufficient to have one of the variables equal to zero, and the other less than a prespecified tolerance. The tolerance on the electric field is 50 V/cm, where the peak electric field is over

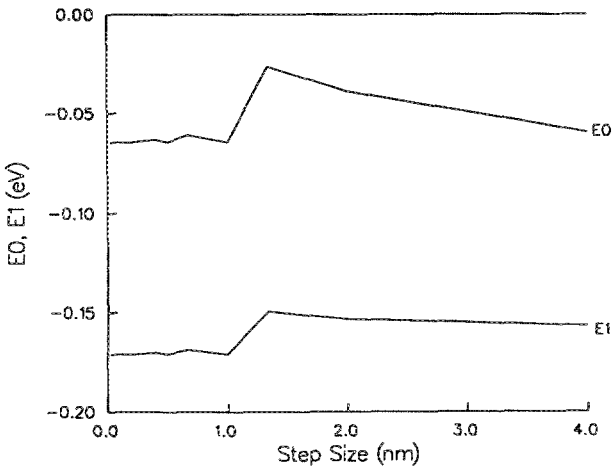

FIG. 3. E_0 and E_1 for a sample 5-nm quantum well. For a shell thickness of less than 1 nm, the solutions are relatively stable.

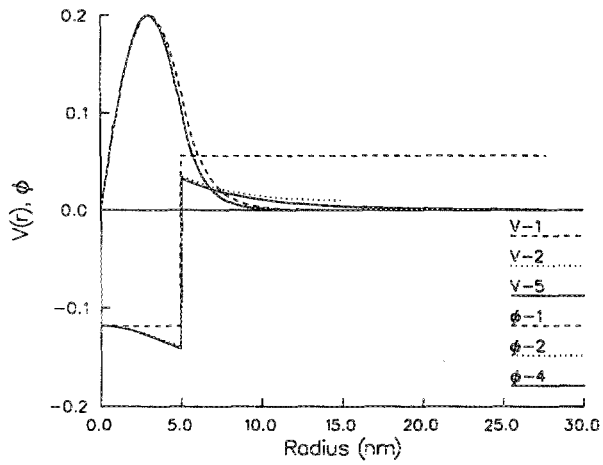

FIG. 4. Well potential and wave function for repeated iterations. ϕ is the probability $\psi^2 r$. The units on ϕ are arbitrary. Equilibrium is achieved after only five iterations. Only the fourth ϕ is calculated as the fifth V, which uses $\phi - 4$, is accepted as a solution.

100 000 V/cm. The tolerance on the potential is less than 1% of kT at 300 K. It is often possible to "surround" the exact equilibrium point to within 5.0×10^{-6} V.

At equilibrium, successive iterations of Schrödinger's and Poisson's equations should produce the same solutions. Initially, the case is different. The first time that Schrödinger's equation is solved, we must use a simple approximation to the shape of the well. Using the bound-electron data for a cylindrical quantum-well potential, we can then make a first attempt at solving Poisson's equation. Using the new shape of the well we can re-solve Schrödinger's equation and get improved information about the bound states. Figure 4 shows the shape of the well after repeated solutions of both Schrödinger's and Poisson's equation. This process is repeated until the first bound energy state is steady to within 1%

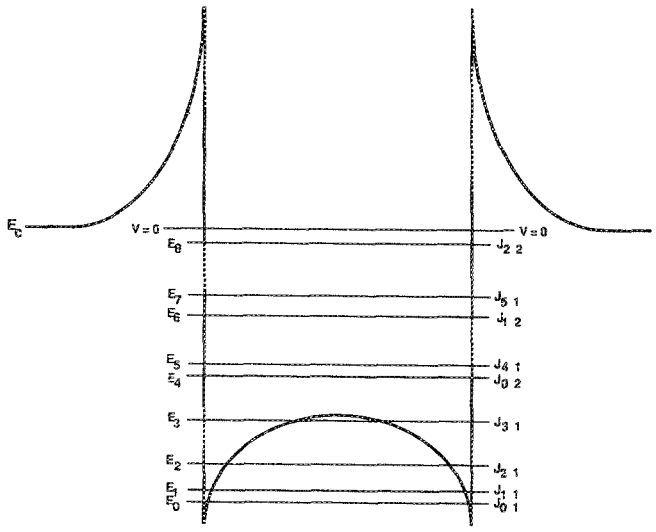

FIG. 5. Energy level ordering in a 20-nm-radius well at 300 K, with $N_d = 1 \times 10^{18}$ cm^{-3}. The labels J_{nm} refer to the mth solution of the nth order radial equation.

between successive solutions. The only parameter that must be varied to approach equilibrium is the potential at r_c. After equilibrating the energy, the solution of Poisson's equation can be examined and used to estimate a new value of $V(r_c)$. A simple Newton's method, coupled with a bisector, will adjust the potential at r_c until equilibrium is achieved.

The energy spectrum for the quantum wire is not as simple as the case for a quantum well. For each order of the Bessel-like functions n, there can be more than one solution of the radial equation. To rank the solution of each order n, we introduce the quantum number m. Figure 5 shows the ordering of the energy levels in a 20-nm-radius well. The radial probability distributions are plotted for the four bound states of a 10-nm-radius well in Fig. 6. Increasing the order of the Bessel function n has the effect of shifting the first maximum in the probability distribution away from the origin, while increasing m has the effect of pulling more zeros of the probability distribution into the well. One caveat in interpreting the effect of increasing n and m is that $\psi^2 \neq 0$ at $r = 0$ for $n = 0$, while $\psi^2 = 0$ at $r = 0$ for all $n > 0$. The probability distribution, however, is $\psi^2 r$, which introduces a zero at the origin for all n, independent of the properties of the Bessel functions.

V. RESULTS

The parameters that were varied during the study of the quantum wire were the AlAs mole fraction x, the AlGaAs doping N_d, the quantum-wire radius r_w, and the spacer layer thickness d_s. The AlAs mole fraction was chosen to vary between 0.1 and 1.0 to cover the maximum range for reasonable confinement. The AlGaAs doping was varied between 5.0×10^{15} and 5.0×10^{18} cm^{-3}, which approaches the background limit at the low end, and at the high end is limited by Fermi-level pinning. The quantum-wire radius was varied from 3 to 20 nm, with 3 nm representing the minimum level for practical confinement, and at 20 nm the number of confined states becomes large. Finally, the spacer layer thickness was varied from 0 to 21 nm. An increase in spacer layer thickness results in reduced remote donor scattering at the expense of the transferred electron density. The prototype wire has an AlAs mole fraction of 0.25, a doping level of 1.0×10^{18} cm^{-3}, a radius of 10 nm, and a spacer layer thickness of 0 nm. As the individual parameters are varied, the remaining three assume the prototype values.

The first parameter that was investigated was the AlAs mole fraction x in the barrier AlGaAs. The mole fraction

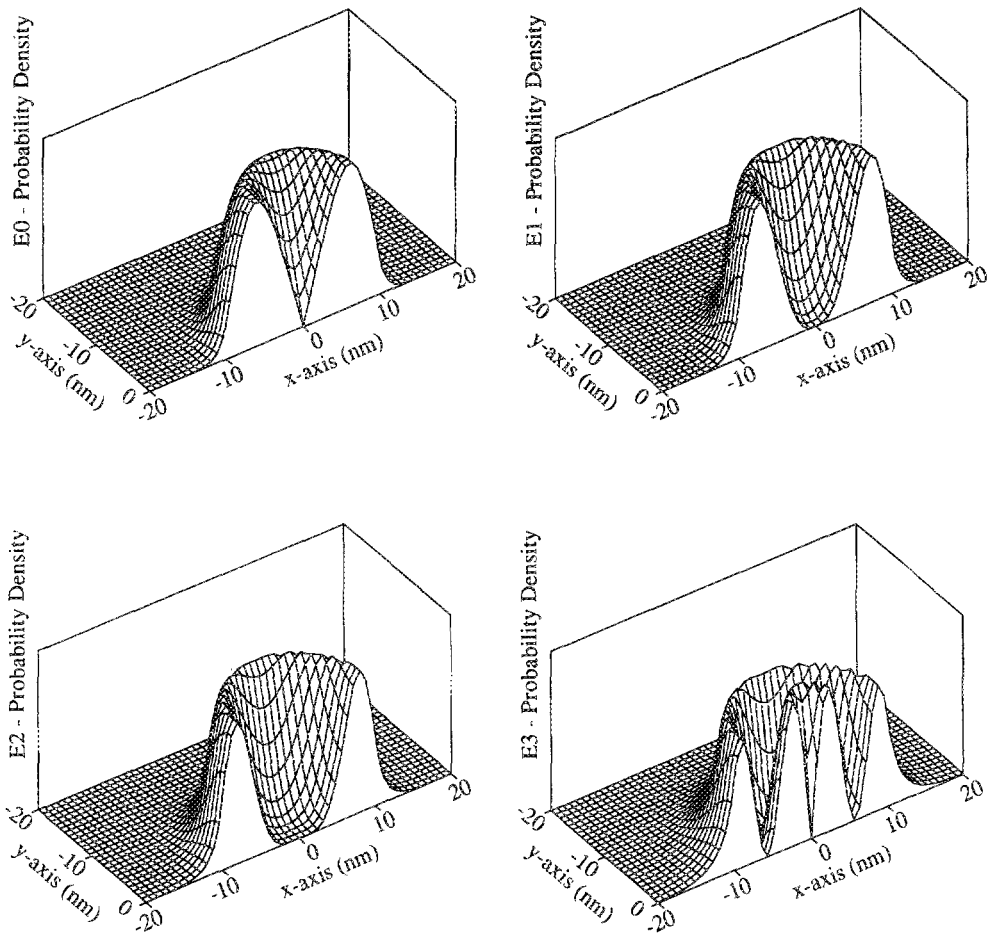

FIG. 6. Probability functions for the four bound states in a 10-nm-radius well at 300 K with $N_d = 1\times10^{18}$ cm^{-3}. The scaling on the probability axis is arbitrary.

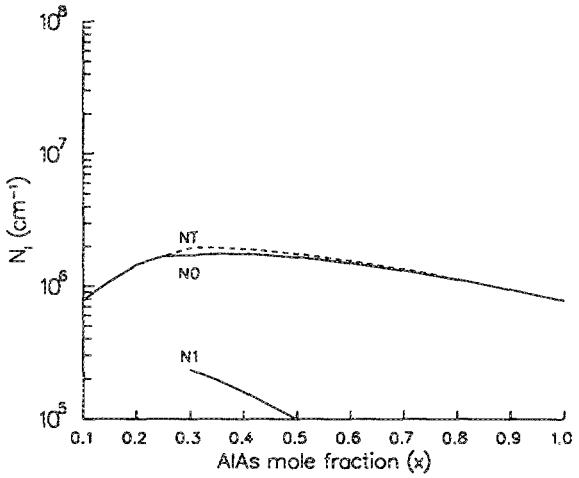

FIG. 7. Transferred electron density (cm^{-1}) vs aluminum arsenide mole fraction (x) for a 5-nm-radius quantum well. The temperature is 300 K, and the AlGaAs doping is 1.0×10^{18} cm^{-3}.

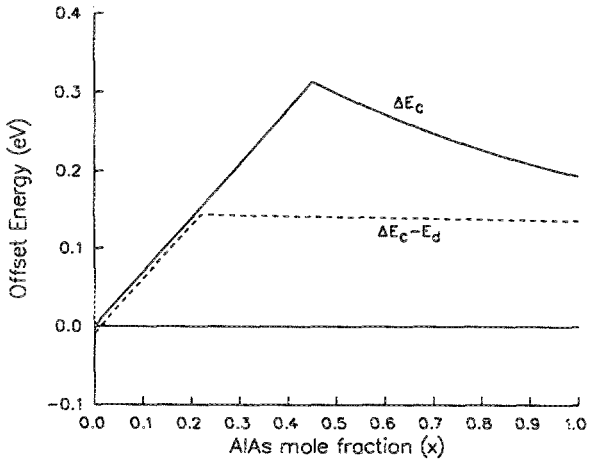

FIG. 9. Conduction-band offset and donor ionization energy in AlGaAs vs aluminum arsenide mole fraction.

was varied from 0.1 to 1.0 for wells of radius 5 and 10 nm. Both cases were done at 300 K. Figures 7 and 8 show these results. Both plots show an increase in electron density with increasing mole fraction up to $x = 0.3$. During the initial increase, the conduction-band offset is increasing, resulting in deeper bound states with higher occupation. After $x = 0.3$, both curves begin to fall off. There are two effects that are responsible for the fall in transferred electron density, the donor ionization energy variation with x, and the conduction-band offset variation with x. The donor ionization energy versus x (Ref. 14) and the conduction-band offset versus x are shown in Fig. 9. For AlAs mole fractions above 0.22, the donor ionization energy begins to increase rather sharply. This lowers the bulk AlGaAs Fermi level, which in turn will decrease the subband occupation within the well. At compositions greater than $x = 0.45$, the conduction-band offset begins to fall. Although the donor energy does begin to fall for composition greater than 0.45, the sharp decrease in the conduction-band offset dominates, and the transferred electron density continues to decrease.

It is convenient that the peak modulation-doped density occurs near $x = 0.30$. It is easiest to grow AlGaAs for low compositions, x below 0.30.[15] The persistent photoconductivity effect is also reduced for lower mole fractions. Although one can choose almost any aluminum fraction and still achieve close to maximum modulation doping, technological factors favor choosing AlAs mole fractions near 0.25.

The next parameter of interest is the donor doping level in the AlGaAs. Figures 10 and 11 show the transferred electron density in the prototype structure at 77 and 300 K, respectively. At all doping levels, the 77-K plot shows a consistently higher electron density within the well, and the rel-

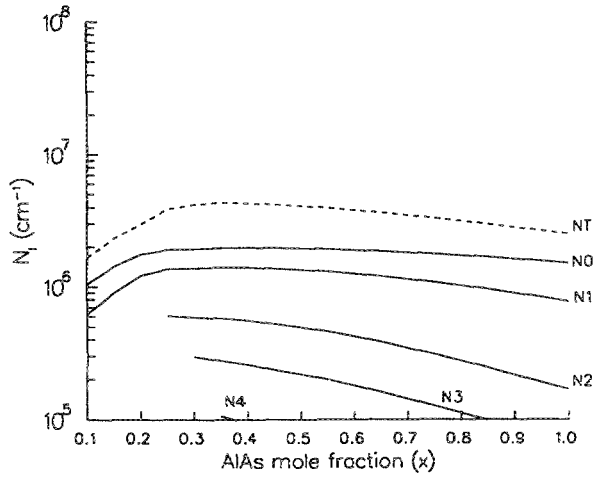

FIG. 8. Transferred electron density (cm^{-1}) vs aluminum arsenide mole fraction (x) for a 10-nm-radius quantum well. The temperature is 300 K, and the AlGaAs doping is 1.0×10^{18} cm^{-3}.

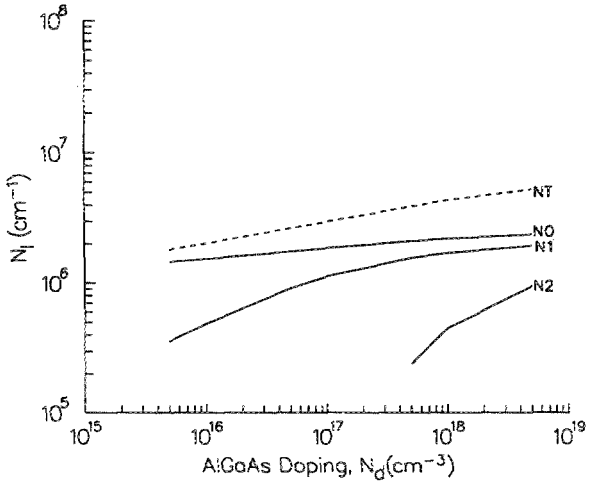

FIG. 10. Transferred electron density (cm^{-1}) vs AlGaAs doping. The temperature is 77 K, the well radius is 10.0 nm, and the aluminum fraction is 0.25.

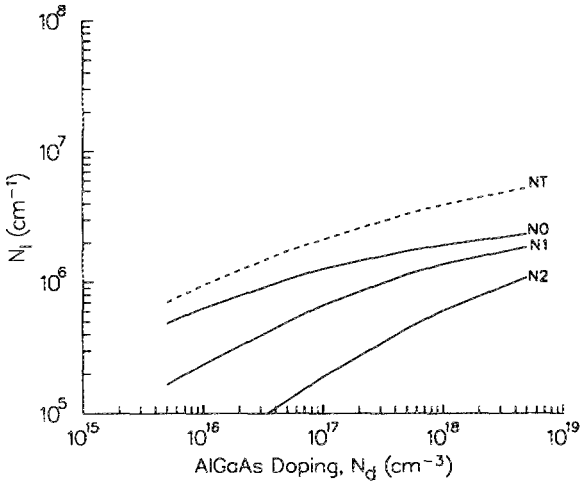

FIG. 11. Transferred electron density (cm^{-1}) vs AlGaAs doping. The temperature is 300 K, the well radius is 10.0 nm, and the aluminum fraction is 0.25.

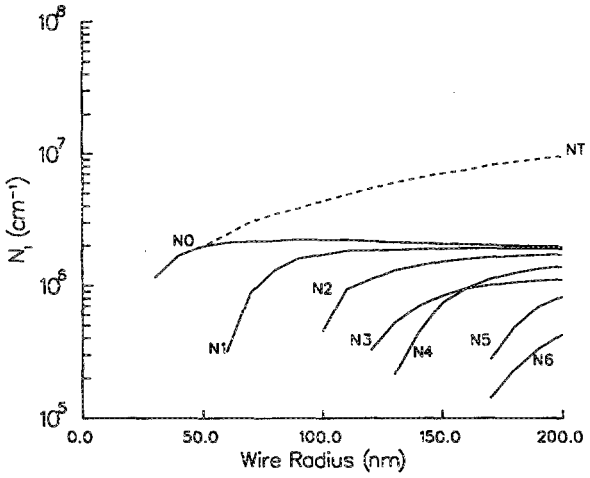

FIG. 13. Transferred electron density (cm^{-1}) vs well radius. The temperature is 77 K, the aluminum arsenide mole fraction is 0.25, and the AlGaAs doping is 1.0×10^{18} cm^{-3}.

ative subband populations shift to favor the lower subbands, E_0 and E_1 at the expense of E_2. The temperature dependence illustrated in Figs. 10 and 11 is primarily a result of electron freezeout in the AlGaAs host layer as the temperature is reduced below 300 K. Figure 12 shows the temperature dependence of the Fermi level in the AlGaAs, relative to the intrinsic level, at several doping levels. As the temperature is lowered, E_f moves toward $\frac{1}{2}(E_c - E_d)$. Raising the Fermi level in the bulk raises the Fermi level through the well, thereby increasing the transferred electron density. Figure 12 also shows less dependence of E_f on N_d at 77 K, which is reflected by the relative independence of the transferred electron density from the doping level in Fig. 10. This implies that it is possible to grow a nearly intrinsic structure and still achieve significant electron densities within the well.

Figures 13 and 14 show the variation in linear density with well radius r_w at 77 and 300 K, respectively. As before, we expect the 77-K plot to show a consistently higher modulation-doped density over the 300 K case. As the radius of the well is increased, higher-order subbands are introduced into the system. These subbands increase their population as the well radius is further increased. The zeroth-order subband actually begins to lose electrons, as the higher-order subbands are populated. There are seven subbands at a well radius of 20 nm. If the well radius is continually increased, a point will be reached when the bound-state energies begin to mix and form a continuum; at this point the two-dimensional confinement is lost.

At this point it is interesting to compare the charge transfer efficiency of the quantum wire to that of an AlGaAs/GaAs single heterojunction structure. The comparison is not entirely appropriate, as the proper analog is a double heterojunction; however, the single heterojunction supports the existing field-effect transistor technology and

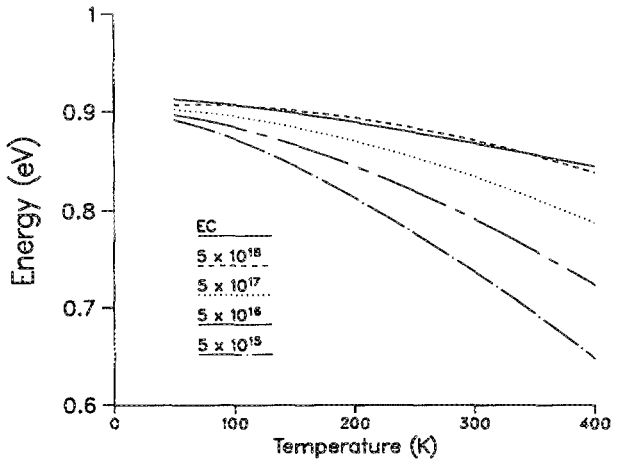

FIG. 12. Fermi level in the AlGaAs as a function of both temperature and doping. The intrinsic level is defined as 0 eV, and the aluminum arsenide mole fraction is 0.25.

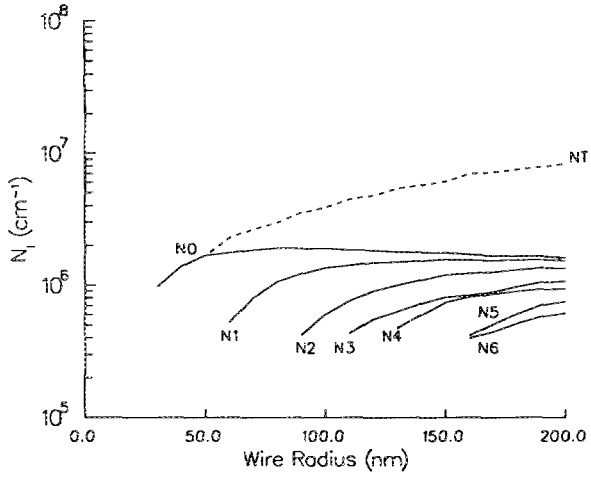

FIG. 14. Transferred electron density (cm^{-1}) vs well radius. The temperature is 300 K, the aluminum arsenide mole fraction is 0.25, and the AlGaAs doping is 1.0×10^{18} cm^{-3}.

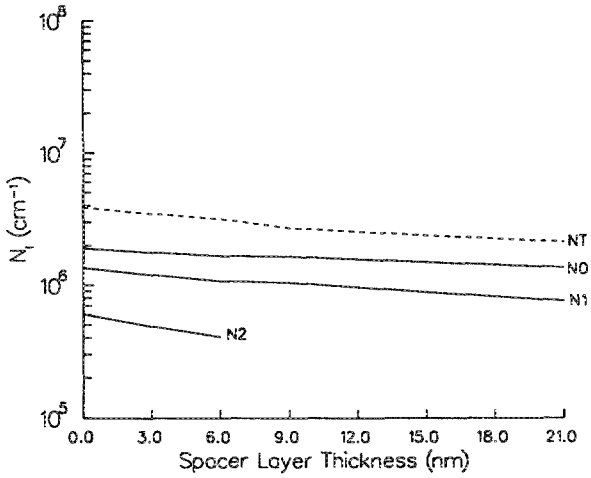

FIG. 15. Transferred electron density (cm^{-1}) vs spacer layer thickness. The aluminum arsenide mole fraction is 0.25, the temperature is 300 K, the AlGaAs doping is 1.0×10^{18} cm^{-3}, and the well radius is 10.0 nm.

has been widely modeled. To obtain the transfer efficiency, we normalize the wire density by $N_d^{1/3}$ and the two-dimensional density of the heterojunction structure by $N_d^{2/3}$. For heterojunction structures appropriate to transistor applications, the density ratio is less than 1. For the quantum wire the ratio is on average 5, reaching a maximum of 9.4 in the study for $T=300$ K, $r_w=20$ nm, and $N_d=1\times10^{18}$ cm^{-3}. At most, the appropriate double-heterostructure quantum-well analog should only double the transfer efficiency, leading to the conclusion that the reduced dimensionality of the wire system leads to more efficient charge collection.

The final parameter of interest investigated here is the thickness of a spacer layer surrounding the quantum wire. This arrangement is designed to parallel the design parameter important to transistor design in single-heterojunction structures. The spacer layer is an undoped region of AlGaAs immediately surrounding the wire and providing further separation between the electrons and donor atoms. The increased separation results in increased mobility along the wire axis. Figure 15 shows the effects of increasing the spacer layer thickness. As the spacer layer thickness is increased, the transferred electron density decreases. If we were to let the spacer layer thickness approach infinity, then the problem would simply shift to a quantum wire surrounded by intrinsic AlGaAs.

VI. CONCLUSIONS

In order to investigate one-dimensional quantum wires, a self-consistent solution of Poisson's and Schrödinger's equations is required and is implemented in cylindrical coordinates. A transfer matrix method used in solving Schrödinger's equation is described. We present the results of a systematic variation of the relevant parameters over the maximum range believed to be a practical interest. This is intended to provide a guide to the design of quantum wires for experimentalists. Presumably, the results are qualitatively similar to those obtained from an analysis of square or triangular wires. We have shown that "large" transferred electron densities may be obtained for low doping and large spacer layer thicknesses, improving the chances of obtaining ballistic transport.

ACKNOWLEDGMENTS

The authors would like to thank Dr. J. East for a critical review of this manuscript. One of the authors (M. E. S.) would like to thank John Loehr for numerous discussions about numerical methods and David Pehlke for his help on the Apollo computers. This work was supported by the U.S. Army Research Office.

APPENDIX A: GaAs AND AlGaAs MATERIAL DATA

To prevent confusion that might arise from gathering material data from many different sources, the band structure variation is that compiled by Casey and Panish.[16] Table I gives a summary of the data used.

In the table, the effective masses given are the density-of-state effective masses. This means that the number of equivalent valley minima is already included in the number given. The value given for the holes includes effects from the light and heavy holes. To include the effects of temperature upon the band positions, all of the bands should be referenced to the gamma valley conduction band in GaAs. To first order, it is assumed that all the bands have roughly the same temperature dependence of the gamma valley. The equation below gives the gamma valley band gap in GaAs as a function of temperature:

$$E_g^{\Gamma}=1.519-\frac{5.405\times10^{-4}T^2}{204+T}\ \text{eV}, \tag{A1}$$

where T is the temperature in Kelvin.

The conduction-band offsets between the GaAs and AlGaAs was calculated by assuming a valence-band discontinuity given by the following equation[17]:

$$\Delta E_v=0.55x,$$
$$\Delta E_c=\Delta E_g-\Delta E_v.$$

The last items that must be considered are the donor and acceptor activation energies. Figure 9 shows the dependence of the donor activation energy on the aluminum mole fraction x.[14] The experimentally determined donor activation

TABLE I. GaAs and AlGaAs material data.

	GaAs	$Al_xGa_{1-x}As$
E_g^{Γ}	1.424 eV	$1.424+1.247x$ eV $(0<x<0.45)$ $1.424+1.247x+1.147(x-0.45)^2$ eV $(0.45<x<1.0)$
E_g^{L}	1.708 eV	$1.708+0.642x$ eV
E_g^{X}	1.900 eV	$1.900+0.125x+0.143x^2$ eV
m_n^{Γ}	$0.067m_0$	$(0.067+0.083x)m_0$
m_n^{L}	$0.55m_0$	$(0.55+0.12x)m_0$
m_n^{X}	$0.85m_0$	$(0.85-0.07x)m_0$
m_p	$0.48m_0$	$(0.48+0.31x)m_0$

energy, derived assuming Casey and Panish's band structure, is described below:

$$E_d = E_g^{\Gamma}(x) - 0.09 \text{ eV} \quad (0<x<0.22)$$
$$= E_G^{\Gamma}(x=0) + 0.148 + 0.54x \text{ eV} \quad (0.22<x<1.0), \tag{A2}$$

where the temperature dependence of the donor level is assumed to be similar to that of the direct gamma gap in GaAs. The acceptor activation energy is assumed to be constant for all compositions and is equal to 50 meV.

APPENDIX B: BOUNDARY CONDITION EQUATIONS FOR SCHRÖDINGER'S EQUATION

In the text, the boundary conditions were defined for the cylindrical Schrödinger's equation. Only one of the four possibilities was derived at that time. In this appendix the results for the other three possibilities will be presented.

Returning to the definition of a region, we find that there are two types of regions; the first being oscillatory in nature, type I, and the second being of the decay type, type II. The four possible boundary conditions that can arise are I-I, I-II, II-I, and II-II, Earlier, the I-II arrangement was developed. For clarity, the equations that must be satisfied at the boundary are repeated below:

$$R_l(a) = R_r(a), \tag{B1}$$

$$\frac{R_l'(a)}{m_l(a)} = \frac{R_r'(a)}{m_r(a)} \tag{B2}$$

where $r=a$ is the boundary, the subscripts r and l denote the right and left sides of the boundary, respectively, and the wave function R is defined below for both types of regions:

$$R_{\rm I}(r) = AJ_n(\kappa_{\rm I} r) + BN_n(\kappa_{\rm I} r), \tag{B3}$$
$$R_{\rm II}(r) = CI_n(\chi_{\rm II} r) + DK_n(\chi_{\rm II} r), \tag{B4}$$

where the coefficients A, B, C, and D are to be determined by the boundary conditions or the initial conditions. The propagation coefficients κ and χ are given below:

$$\kappa_{\rm I}^2 = -\chi_{\rm II}^2 = (2m_l/\hbar^2)(E - V_l). \tag{B5}$$

When developing the equations relating the coefficients A, B, C, and D, it will be assumed that A and B are the coefficients of the wave function on the left side of the boundary. The wave function on the left side is already known, as we are propagating outwards from $r=0$. The initial conditions for the first region have already been described in the text. The wave function on the left side will be R_l, with the wave function on the right side being referred to as R_r. All of the Bessel-like functions carry the subscript n, which is a result of the angular solution. The propagation coefficients κ and χ have subscripts r and l, referencing them to the wave functions R_r and R_l.

Now we can develop the equations for the I-I interface. Putting the wave functions into the boundary conditions we arrive at the following equations:

$$AJ_n(\kappa_l a) + BN_n(\kappa_l a) = CJ_n(\kappa_r a) + DN_n(\kappa_r a), \tag{B6}$$

$$m_r[AJ_n'(\kappa_l a) + BN_n'(\kappa_l a)] = m_l[CJ_n'(\kappa_r a) + DN_n'(\kappa_r a)]. \tag{B7}$$

The final step is to solve the coefficients C and D:

$$C = \frac{A[m_r J_n'(\kappa_l a)N_n(\kappa_r a) - m_l J_n(\kappa_l a)N_n'(\kappa_r a)]}{m_l J_n'(\kappa_r a)N_n(\kappa_r a) - m_l J_n(\kappa_r a)N_n'(\kappa_r a)} + \frac{B[m_r N_n'(\kappa_l a)N_n(\kappa_r a) - m_l N_n(\kappa_l a)N_n'(\kappa_r a)]}{m_l J_n'(\kappa_r a)N_n(\kappa_r a) - m_l J_n(\kappa_r a)N_n'(\kappa_r a)}, \tag{B8}$$

$$D = \frac{A[m_r J_n'(\kappa_l a)J_n(\kappa_r a) - m_l J_n(\kappa_l a)J_n'(\kappa_r a)]}{m_l N_n'(\kappa_r a)J_n(\kappa_r a) - m_l N_n(\kappa_r a)J_n'(\kappa_r a)} + \frac{B[m_r N_n'(\kappa_l a)J_n(\kappa_r a) - m_l N_n(\kappa_l a)J_n'(\kappa_r a)]}{m_l N_n'(\kappa_r a)J_n(\kappa_r a) - m_l N_n(\kappa_r a)J_n'(\kappa_r a)}. \tag{B9}$$

The derivations for the II-I and II-II interfaces are identical, and therefore only the final results for both cases will be presented.The equations related the coefficients C and D to A and B for the II-I interface are given below:

$$C = \frac{A[m_r I_n'(\chi_l a)N_n(\kappa_r a) - m_l I_n(\chi_l a)N_n'(\kappa_r a)]}{m_l J_n'(\kappa_r a)N_n(\kappa_r a) - m_l J_n(\kappa_r a)N_n'(\kappa_r a)} + \frac{B[m_r K_n'(\chi_l a)N_n(\kappa_r a) - m_l K_n(\chi_l a)N_n'(\kappa_r a)]}{m_l J_n'(\kappa_r a)N_n(\kappa_r a) - m_l J_n(\kappa_r a)N_n'(\kappa_r a)}, \tag{B10}$$

$$D = \frac{A[m_r I_n'(\chi_l a)J_n(\kappa_r a) - m_l I_n(\chi_l a)J_n'(\kappa_r a)]}{m_l N_n'(\kappa_r a)J_n(\kappa_r a) - m_l N_n(\kappa_r a)J_n'(\kappa_r a)} + \frac{B[m_r K_n'(\chi_l a)J_n(\kappa_r a) - m_l K_n(\chi_l a)J_n'(\kappa_r a)]}{m_l N_n'(\kappa_r a)J_n(\kappa_r a) - m_l N_n(\kappa_r a)J_n'(\kappa_r a)}. \tag{B11}$$

Finally, the equations for the II-II interface are given below:

$$C = \frac{A[m_r I_n'(\chi_l a)K_n(\chi_r a) - m_l I_n(\chi_l a)K_n'(\chi_r a)]}{m_l I_n'(\chi_r a)K_n(\chi_r a) - m_l I_n(\chi_r a)K_n'(\chi_r a)} + \frac{B[m_r K_n'(\chi_l a)K_n(\chi_r a) - m_l K_n(\chi_l a)K_n'(\chi_r a)]}{m_l I_n'(\chi_r a)K_n(\chi_r a) - m_l I_n(\chi_r a)K_n'(\chi_r a)}, \tag{B12}$$

$$D = \frac{B[m_r K_n'(\chi_l a)K_n(\chi_r a) - m_l K_n(\chi_l a)K_n'(\chi_r a)]}{m_l I_n'(\chi_r a)K_n(\chi_r a) - m_l I_n(\chi_r a)K_n'(\chi_r a)}, \quad \frac{B[m_r K_n'(\chi_l a)K_n(\chi_r a) - m_l K_n(\chi_l a)K_n'(\chi_r a)]}{m_l I_n'(\chi_r a)K_n(\chi_r a) - m_l I_n(\chi_r a)K_n'(\chi_r a)}, \tag{B13}$$

[1] S. E. Laux, D. J. Frank, and F. Stern, Surf. Sci. **196**, 101 (1988).
[2] G. Timp, A. M. Chang, P. Makiewich, R.Behringer, J. E. Cunningham, T. Y. Chang, and R. E. Howard, Phys. Rev. Lett. **59**, 732 (1987).
[3] D. A. Wharam, T. J. Thornton, R. Newbury, M. Pepper, H. Ahmed, J. E. F. Frost, D. G. Hasko, D. C. Peacock, D. A. Ritchie, and G. A. C. Jones, J. Phys. C **21**, L209 (1988).
[4] G. Kirczenow, Phys. Rev. B **38**, 10958 (1988).
[5] H. Sakaki, Jpn. J. Appl. Phys. **19**, L735 (1980).
[6] M. Sweeney, J. Xu, and M. Shur, Superlatt. Microstruc. **4**, 623 (1988).

[7]X. Aymerich-Humet, F. Serra-Mestres, and J. Millan, J. Appl. Phys. **54**, 2850 (1983).
[8]S. M. Sze, *Physics of Semiconductor Devices*, 2nd ed. (Wiley, New York, 1981), Chap. 1.4.
[9]R. V. Churchill, *Fourier Series and Boundary Value Problems*, 2nd ed. (McGraw-Hill, New York, 1969).
[10]J. M. Blatt, J. Comput. Phys. **1**, 382 (1967).
[11]E. Buendia and R. Guardiola, J. Comput. Phys. **60**, 561 (1985).
[12]R. Perez-Alvarez, J. L. Parra-Santiago, and P. Pajon-Suarez, Phys. Status Solidi B **147**, 127 (1988).
[13]M. Abramowitz and I. A. Stegun, *Handbook of Mathematical Functions*, tenth printing (National Bureau of Standards, Washington, D. C., 1972).
[14]N. Chand, T. Henderson, J. Klem, W. T. Masselink, R. Fischer, Y. C. Chang, and H. Morkoç, Phys. Rev. B **3**, 4481 (1984).
[15]H. Morkoç, T. J. Drummond, W. Koop, and R. Fischer, J. Electrochem. Soc. **129**, 824 (1982).
[16]H. C. Casey, Jr. and M. B. Panish, *Heterostructure Lasers—Part A* (Academic, Orlando, 1978).
[17]J. Batey and S. L. Wright, J. Appl. Phys. **59**, 200 (1986).